Improved Accuracy of the Asymmetric Second-Order Vegetation Isoline Equation over the RED–NIR Reflectance Space

Munenori Miura [1], Kenta Obata [2], Kenta Taniguchi [1] and Hiroki Yoshioka [1,*]

[1] Department of Information Science and Technology, Aichi Prefectural University, 1522-3 Ibara, Nagakute, Aichi 480-1198, Japan; id151003@cis.aichi-pu.ac.jp (M.M.); id151002@cis.aichi-pu.ac.jp (K.T.)

[2] National Institute of Advanced Industrial Science and Technology, The Institute of Geology and Geoinformation, Central 7, 1-1-1, Higashi, Tsukuba, Ibaraki 305-8567, Japan; kenta.obata@aist.go.jp

* Correspondence: yoshioka@ist.aichi-pu.ac.jp; Tel.: +81-561-76-9884

Abstract: The relationship between two reflectances of different bands is often encountered in cross calibration and parameter retrievals from remotely-sensed data. The asymmetric-order vegetation isoline is one such relationship, derived previously, where truncation error was reduced from the first-order approximated isoline by including a second-order term. This study introduces a technique for optimizing the magnitude of the second-order term and further improving the isoline equation's accuracy while maintaining the simplicity of the derived formulation. A single constant factor was introduced into the formulation to adjust the second-order term. This factor was optimized by simulating canopy radiative transfer. Numerical experiments revealed that the errors in the optimized asymmetric isoline were reduced in magnitude to nearly 1/25 of the errors obtained from the first-order vegetation isoline equation, and to nearly one-fifth of the error obtained from the non-optimized asymmetric isoline equation. The errors in the optimized asymmetric isoline were compared with the magnitudes of the signal-to-noise ratio (SNR) estimates reported for four specific sensors aboard four Earth observation satellites. These results indicated that the error in the asymmetric isoline could be reduced to the level of the SNR by adjusting a single factor.

1. Introduction

Estimation of biophysical parameters from remotely sensed reflectance requires calibration [1], inter-comparison of reflectance spectra [2] and derived data products [3]. Parameter retrieval based on those calibration efforts has been a major goal of land analysis disciplines [4]. The outcomes of such efforts provide crucial information about local and global areal coverage, information that is used in a wide range of applications [5]. Although numerous investigations have reported the development and improvement of biophysical parameter retrieval algorithms, many of these algorithms involve simple algebraic band manipulations known as spectral vegetation indices (VIs) [6,7]. A variety of VI models have been investigated for their robustness against both internal and external influences [8–15].

A key component of VI model development is the relationship between two reflectances of different bands obtained under fixed biophysical parameter conditions. This relationship produces a reflectance spectrum trajectory in a reflectance subspace attributed to a fixed biophysical parameter value; therefore, this relationship is known as a vegetation isoline. The concept of a vegetation isoline

has been used repeatedly to develop optimal VI models [8,9,12,16] and to investigate their robustness against external factors [17,18]. The isoline concept has been directly used to retrieve leaf area index and the fraction of vegetation cover [19,20]. In recent years, the concept has been applied to the inter-sensor calibration of VIs [21,22].

From the application point of view, understanding of band-to-band relationship would provide information about land cover dependency of calibration coefficients. In retrievals of biophysical parameter, an isoline equation with higher accuracy would lead to better results in retrieved parameters. Moreover, biophysical parameters vary along with the evolution of phenology, which eventually influence on reflectance spectra. Since the derived coefficients of the vegetation isoline depend on the biophysical parameters, the phenology is also related to the variation of the vegetation isoline.

Significant efforts have been devoted toward deriving useful analytical formulas based on a model of radiative energy transfer. These derivations used a representation of the top-of-canopy (TOC) reflectance spectrum consisting of photons that were directly reflected by the canopy layer. Because this portion of the reflectance spectrum does not reach the soil surface beneath the canopy, it is called the zero-th order interaction term. Photons that reached the soil surface and were reflected back to the canopy layer by the soil surface only once contributed to the measured reflectance. The 'one-time reflected' contributions comprised the first-order interaction term. Analogously, the reflectance spectrum consisting of photons reflected by the soil surface n times was defined as the n-th-order interaction term. The vegetation isoline equations were derived by truncating the second- and higher-order interaction terms. For this reason, the derived isolines are a first-order approximation of the vegetation isoline.

The approximation order determines the accuracy of the derived isoline equations. The accuracy of the isoline has been improved by deriving several approximations that considered the second-order terms. The accuracy has been improved by including higher-order terms. The drawback of this inclusion is that the analytical representation is complex. Complex representations hinder the employment of isoline formulations in applications of various types. It would be beneficial to identify ways of improving the isoline approximation accuracy while maintaining the simplicity of the derived formulation.

In a previous study, we proposed a derivation technique for satisfying these requirements simultaneously [23]. During the derivation, we included the second-order interaction term only in the near-infrared band instead of retaining the second-order term in the red band. This asymmetric approximation form dramatically improved the accuracy of the derived isoline equation.

This study advanced the investigation one step further. The objective was to introduce a technique for improving the accuracy of the asymmetric isoline equations by optimizing a single factor. The goal of this improvement was to reduce the errors in the vegetation isoline equivalent to a value equal to or smaller than the error induced by the inherent signal-to-noise ratio (SNR) of the existing sensors. The accuracy improvements obtained in this study were validated using a radiative transfer model of a system of vegetation and soil layers, the PROSAIL model [24,25]. After optimizing a single factor in the asymmetric approximation of the vegetation isoline equation, the error levels of the improved isoline equations are discussed by comparing the resulting errors with those computed directly from the signal-to-noise ratios of four existing sensors.

2. Background

In this section, two forms of the vegetation isoline equation are introduced. The magnitudes of the errors in the isoline equations differed between the two equations and were characterized numerically.

2.1. Two Approximations of the Vegetation Isoline Equations

The simplest form of the vegetation isoline equation was derived by truncating the soil–canopy interaction terms at the first-order (single interaction) [26]. The resulting equation was simple, which

is advantageous for various applications [17–19,21,22,27–31]. The first-order isoline equation may be written (with the truncation term ϵ_1) as:

$$\rho_N = a\gamma_1\rho_R + D_1 + \epsilon_1, \tag{1}$$

where γ_1 and D_1 are defined by:

$$\gamma_1 = \frac{\overline{T_N^2}}{\overline{T_R^2}}, \tag{2}$$

$$D_1 = b\overline{T_N^2} + \omega\left(\rho_{vN} - a\gamma_1\rho_{vR}\right). \tag{3}$$

The fraction of vegetation cover (FVC) is represented by ω, and the variables ρ_R and ρ_N represent the TOC reflectance in the red and NIR bands, respectively. The variables ρ_{vR} and ρ_{vN} represent the 'pure' canopy reflectances independent of the soil surface beneath the canopy layer. Finally, $\overline{T_R^2}$ and $\overline{T_N^2}$ represent the area-averaged two-way transmittances (T_R^2 and T_N^2), defined by:

$$\overline{T_R^2} = \omega T_R^2 + 1 - \omega, \tag{4}$$

$$\overline{T_N^2} = \omega T_N^2 + 1 - \omega. \tag{5}$$

These variables are explained in additional detail elsewhere [17,21,23].

The second form of the vegetation isoline was derived by only including the interaction terms up to the second-order in the NIR band. The interaction terms in the red band could be expressed using the first-order terms. The asymmetric-order of the approximation in the two bands significantly reduced the error in the isoline relative to the first-order form. The asymmetric form of the vegetation isoline may be written (with the truncation term ϵ_2) as

$$\rho_N = a^2\zeta\rho_R^2 + a\gamma_2\rho_R + D_2 + \epsilon_2, \tag{6}$$

using the definitions:

$$\zeta = \omega T_N^2 R_{vN}/(\overline{T_R^2})^2, \tag{7}$$

$$\gamma_2 = \gamma_1 + \delta_1, \tag{8}$$

$$D_2 = D_1 + \delta_0, \tag{9}$$

$$\delta_0 = \zeta\left(b\overline{T_R^2} - \omega a\rho_{vR}\right)^2, \tag{10}$$

$$\delta_1 = 2\zeta\left(b\overline{T_R^2} - \omega a\rho_{vR}\right). \tag{11}$$

The variable R_{vN} represents the bi-hemispherical reflectance of the canopy layers at the bottom surface, which appears only in the NIR band.

2.2. Errors in the Vegetation Isoline Equations

The asymmetric approximation of the vegetation isoline achieved greater accuracy than the first-order approximation. This fact could be confirmed by conducting a set of numerical simulations and plotting the errors of the two approximated forms. The errors of the two approximated isolines (the first-order and asymmetric-order approximations) were computed assuming a fully covered vegetation canopy, where the value of FVC was set to unity. The PROSAIL model was used to simulate the TOC reflectance by varying the leaf area index (LAI) and soil reflectance spectra (from dark to bright soil). Figure 1a,b shows plots of the error in the first-order isoline and the asymmetric isoline, respectively, as a function of the LAI and soil reflectance. The error in the first-order isoline reached 0.01 in reflectance units as the soil reflectance increased. By contrast, the error in the asymmetric-order

isoline was much smaller than that in the first-order approximation, nearly one order of magnitude smaller, as summarized in our previous study [23].
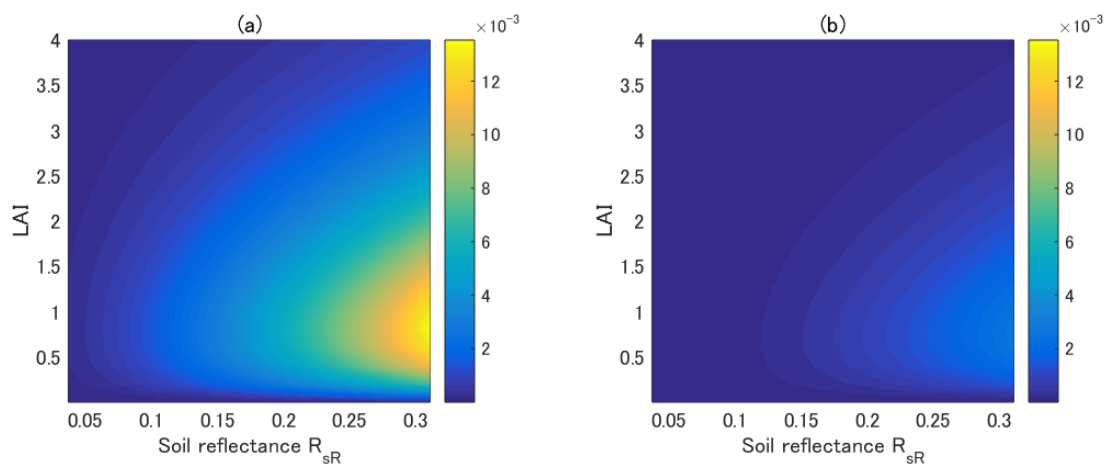

Figure 1. (**a**) Error in the first-order isoline; and (**b**) error in the asymmetric-order isoline. LAI: leaf area index.

We next focused on testing whether the accuracy of the asymmetric approximation was satisfactory from a parameter retrieval point of view. This point was examined by comparing the isoline errors with an error equivalent to the noise level in the reflectance measurements. The comparison was implemented by assuming a simple scenario such that the value of the SNR in the NIR reflectance was 200 and the average value of the NIR reflectance was 0.1 over the entire parameter range. Although this assumption was made for the sake of simplicity, it was a rather conservative assumption because the averaged NIR reflectance is expected to exceed 0.1 in most cases. Under these assumptions, the noise equivalent error could be obtained as 0.0005 in reflectance units over the entire parameter range. With this quick estimate of the noise equivalent error, Figure 2 shows the contour plots of the errors in the first-order approximation (left) and in the asymmetric-order approximation (right). The contour lines that corresponded to the value of 0.0005 are emphasized by thicker black lines in the figures. These results indicated that the error in the first-order approximated isoline mostly exceeded the noise equivalent error for the majority of the cases (represented by the combinations of the LAI and the soil reflectance). Although the error in the asymmetric-order approximation became much smaller than that of the first-order approximation, the errors still exceeded 0.0005, especially at higher soil reflectances. These results suggested that if the asymmetric-order approximated isoline was used for parameter retrieval, the errors in the retrieved results would be larger than the error introduced by the sensor noise. These results indicated that the accuracy of the asymmetric-order approximation required further improvement.
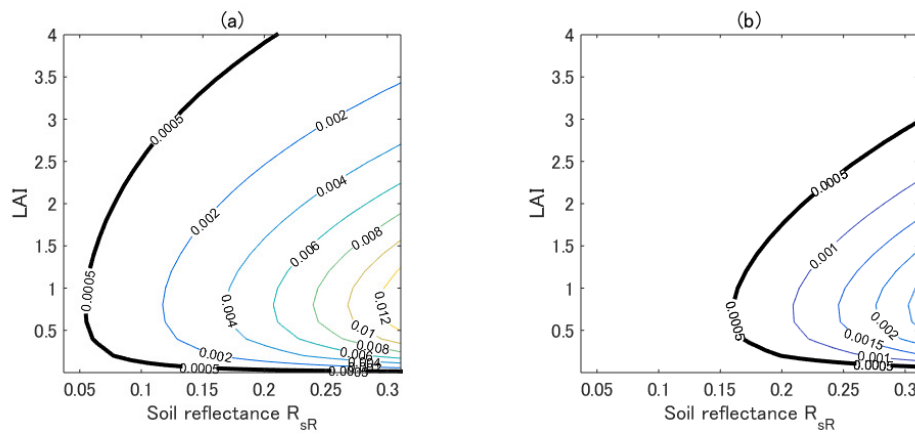
Figure 2. Comparison of the errors in the vegetation isolines with the error (0.0005) computed from the noise corresponding to a signal-to-noise ration (SNR) of 200 at the NIR reflectance of 0.1. (**a**) The error in the first-order isoline; and (**b**) the error in the asymmetric-order isoline. The thick solid lines indicate the contour lines corresponding to 0.0005.

3. Approaches

Improved accuracy was achieved by including the second-order interaction term only in the NIR band. This modification shifted the first-order approximated isoline upward in the reflectance subspace. Figure 3 illustrates this shifting process and the mechanism by which the accuracy was improved via the asymmetric-order approximation. The degree of shifting from the first-order isoline is illustrated as the difference, along the NIR axis, between the blue line and the red line in the figure. This difference remained smaller than the difference between the first-order isoline and the true vegetation isoline (illustrated as the difference between the blue line and the black line). The gap between the asymmetric-order isoline (red line) and the true isoline (black line) must be minimized to achieve the highest accuracy, which this study attempts to address.
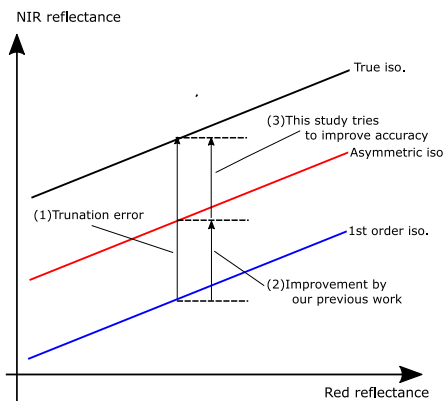
Figure 3. Illustration of the truncation error in the vegetation isoline equations and its improvement by this and previous studies.

This gap could be analytically evaluated by clarifying the difference between the first-order and the asymmetric-order isoline equations. The asymmetric-order approximation form of the vegetation isoline was obtained by neglecting the higher-order interaction term ϵ_2 from Equation (6). The definition of γ_2, Equation (8), was used to express the isoline equation as:

$$\rho_N \approx a^2 \zeta \rho_R^2 + a\gamma_1 \rho_R + a\delta_1 \rho_R + D_1 + \delta_0. \tag{12}$$

After rearranging Equation (12) by noting the form of the first-order isoline Equation (1), the above equation could be transformed to

$$\rho_N \approx a\gamma_1\rho_R + D_1 + \left(a^2\zeta\rho_R^2 + a\delta_1\rho_R + \delta_0\right). \tag{13}$$

The term in the parentheses on the right-hand-side represents the contribution of the asymmetric second-order term, illustrated as the distance between the blue line and the red line in Figure 3. Equation (13) suggests that an adjustment to this distance (overcorrection term) could fill the gap between the red line and the black line, further improving its accuracy.

One way to adjust the overcorrection term is to introduce a factor into the last term of Equation (13). The factor (represented by *k*) introduced into the last term of Equation (13) could be explicitly introduced in the equation,

$$\rho_N \approx a\gamma_1\rho_R + D_1 + k\left(a^2\zeta\rho_R^2 + a\delta_1\rho_R + \delta_0\right). \tag{14}$$

Solving Equation (14) for *k*, we have:

$$k = \frac{\rho_N - (a\gamma_1\rho_R + D_1)}{a^2\zeta\rho_R^2 + a\delta_1\rho_R + \delta_0}. \tag{15}$$

The value of *k* could be computed from Equation (15) for each combination of the model input parameter used for the reflectance simulation. For example, selecting LAI, FVC, and the soil reflectance of the red band R_{sR} as the set of parameters to be varied during the simulation, with the number of grids for each parameter set to 21, a total of 9261 distinctive values of *k* will be obtained. Because *k* depends on a set of parameters, the most accurate way to adjust this scenario is to model the variations in *k* as a function of all parameters. Such an algorithm, however, is not practical to implement at this stage of investigation because one must estimate all input parameters prior to determining *k*. Specifically, LAI, FVC, and the soil reflectance must be estimated to determine *k*. The adjustment approach may be made more practical by determining the optimum constant for *k* according to the following approach, finding a constant value for *k* that minimizes the error of the adjusted isoline, Equation (14), over the entire range of the input parameters. This constant is considered to be the optimum value of *k*, denoted by k_{opt} in this study.

4. Results of the Numerical Simulations

4.1. Parameter Settings for the Numerical Experiments

The variables used in a series of numerical simulations were computed using the canopy radiative transfer code, PROSAIL [25], which consists of the leaf optical properties model (PROSPECT) [32] and the canopy reflectance model (SAIL) [33]. The parameter settings in the simulations are summarized in Table 1. LAI, FVC, and the soil brightness (soil factor) were varied in this study. LAI was varied from 0.0 to 4.0 in 0.2 increments (21 intervals). The soil factor was varied from 0.0 to 1.0 in 0.05 increments (21 variations), which were used to change the mixture ratio of the reflectance spectra of the wet and dry soil provided with the code. The canopy reflectance spectra obtained using PROSAIL were linearly mixed with the soil spectra using the fraction of vegetation cover (FVC), ω, as the weight that was varied from 0.0 to 1.0 in 0.05 increments (21 intervals). The results section focuses on the use of a Spherical model to represent the leaf angle distribution (LAD), with the exception of the simulations presented in Section 4.6, which employs five LAD models (planophile, erectophile, plagiophile, extremophile, and uniform) to examine the effects of the LAD on our simulations. The input parameters in PROSAIL, including the other parameters fixed in this study, are listed in Table 1. The total number of spectra was 9261 (21 × 21 × 21) for a single LAD. (The parameter grids are finer than in our previous study [23].) We employed 655 nm and 865 nm reflectance spectra for the red and

NIR wavelength regions, which corresponded to the center of the red and NIR bands in the Landsat 8 Operational Land Imager (OLI).

Table 1. Input parameters used in the numerical simulations.

Geometry	
Solar zenith angle	30°
Observation zenith angle	10°
Relative azimuth angle	0°
Pixel Heterogeneous Property	
Fraction of vegetation cover (FVC)	0.0–1.0
Canopy Properties	
Leaf area index (LAI)	0.0–4.0
Hotspot size parameter	0.01
Leaf Structural and Chemical Properties	
Leaf angle distribution (LAD)	Spherical, Planophile, Erectophile Plagiophile, Extremophile, Uniform
Leaf mesophyll structure	1.5
Chlorophyll-a and -b	40 μg/cm^2
Carotenoid content	8 μg/cm^2
Leaf mass per area	0.009 g/cm^2
Equivalent water thickness	0.01 cm
Brown pigment content	0
Soil Properties	
Wet soil reflectances at 655 and 865 nm	0.037 and 0.071
Dry soil reflectances at 655 and 865 nm	0.311 and 0.412
Soil factor (mixture ratio of wet and dry soils)	0.0–1.0 [0.0: wet soil; 1.0: dry soil]

4.2. Numerical Procedure Used for the Isoline Parameter Retrieval

The parameters in the isoline equations were computed according to the procedures reported previously [23,26]. $T_{v\lambda}^2$ and $\rho_{v\lambda}$ were determined based on two hypothetical simulations. First, $\rho_{v\lambda}$ was computed using spectrally flat zero reflectances of the soil surface. Subsequently, $T_{v\lambda}$ was approximated using simulated reflectances and a median reflectance of the soil surface, and $\rho_{v\lambda}$ was computed in previous step [26]. The parameter R_{vN}, which was required for the computation of ξ, was obtained by conducting an additional simulation in which the soil spectrum was even brighter than was assumed in the simulation used to compute $T_{v\lambda}$. The soil spectrum was also spectrally flat in this case [23]. In the simulation, the TOC canopy reflectances in the NIR were approximated using first- and second-order interaction terms between the canopy layer and the soil surface,

$$\rho_N \approx \omega \rho_{vN} + \overline{T_N^2} R_{sN} + \omega T_N^2 R_{vN} R_{sN}^2. \tag{16}$$

where R_{sN} represents the bi-hemispherical reflectance of the soil surface for the NIR band. R_{vN} was then derived by solving Equation (16) for R_{vN}. The isoline parameters for the canopy layer were obtained using these variables. The slope and offset of the soil line equation over the red and NIR reflectance spaces used in the isoline parameters were obtained from a linear regression of the reflectance spectra for the wet and dry soils, shown in Table 1 ($a = 1.24$ and $b = 0.026$).

4.3. Variations in k

The dependences of LAI, FVC, and R_{sR} on k were analyzed based on numerical experiments in which the k-value was computed in the previous step using Equation (15). Three experimental conditions were applied to compute k: (1) FVC was varied using three pairs of fixed LAI and R_{sR} values; (2) LAI was varied using three pairs of fixed FVC and R_{sR} values; and (3) R_{sR} was varied using three pairs of fixed FVC and LAI values. The results of the first case are shown in Figure 4a. The k-values

are plotted against FVC for "LAI = 1.0 and R_{sR} = 0.1", "LAI = 2.0 and R_{sR} = 0.1", and "LAI = 2.0 and R_{sR} = 0.2", denoted by the solid, dashed, and dotted lines, respectively. The k-values were relatively insensitive to the changes in FVC. The differences between the k values for FVC = 0.0 and FVC = 0.9 were less than 1%, and the differences for FVC = 0.0 and FVC = 1.0 were less than 3% for each pair of LAI and R_{sR}. The strong dependence of R_{sR} on k was identified from the large differences between the k-value curves obtained at R_{sR} = 0.1 and = 0.2.
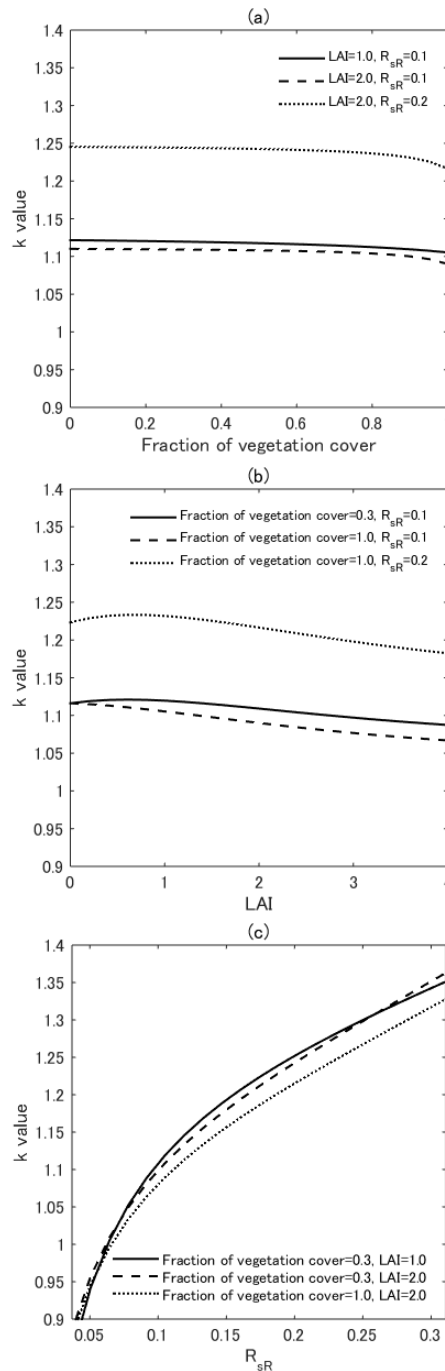
Figure 4. (**a**) Plot of the k-values along with the FVC over three pairs of fixed LAI and R_{sR} (LAI = 1.0 and R_{sR} = 0.1, LAI = 2.0 and R_{sR} = 0.1, and LAI = 2.0 and R_{sR} = 0.2); (**b**) Plot of the k-values along with LAI over three pairs of fixed FVC and R_{sR} (FVC = 0.3 and R_{sR} = 0.1, FVC = 1.0 and R_{sR} = 0.1, and FVC = 1.0 and R_{sR} = 0.2); (**c**) Plot of the k-values along with R_{sR} over three pairs of fixed FVC and LAI (FVC = 0.3 and LAI = 1.0, FVC = 0.3 and LAI = 2.0, and FVC = 1.0 and LAI = 2.0).

Similarly, the k-values were relatively insensitive to LAI, as shown in Figure 4b (results are shown for the second experimental case). These k-values are plotted against LAI for "FVC = 0.3 and R_{sR} = 0.1", "FVC = 1.0 and R_{sR} = 0.1", and "FVC = 1.0 and R_{sR} = 0.2", respectively. The differences between the k-values for LAI = 0.0 and LAI = 4.0 were less than 5%. The differences between the results obtained for R_{sR} = 0.1 and = 0.2 were similarly large, as shown in Figure 4a.

Figure 4c presents the results obtained from the third case, which described the k-values along R_{sR} for "FVC = 0.3 and LAI = 1.0", "FVC = 0.3 and LAI = 2.0", and "FVC = 1.0 and LAI = 2.0", respectively. The k-values showed an approximately 50% increase (from 0.9 to 1.35) with increasing R_{sR}. The differences among the three pairs of LAI and FVC affected the k-value to a much smaller degree than did the differences between the maximum and minimum R_{sR} values. These results indicated that the k-values depended heavily on R_{sR} but were nearly independent of FVC and LAI (greenness level of the vegetation canopy).

4.4. Optimum k-Values (k_{opt})

The k-values were computed using all possible pairs of the input parameters (FVC, LAI, and R_{sR} were changed; LAD was fixed to a spherical model; and all other input parameters were fixed, as shown in Table 1). The optimum value of k was then determined by computing the distances (ϵ) as the errors between the true spectra $\boldsymbol{\rho}$ (including all the higher-order terms) and the vegetation isolines (the adjusted asymmetric isolines by Equation (14)),

$$\epsilon(k) = min(\|\boldsymbol{\rho} - \hat{\boldsymbol{\rho}}(k)\|_2), \tag{17}$$

where $\hat{\boldsymbol{\rho}}(k)$ denotes the spectra on the vegetation isolines for the k-value as the input. Note that $\epsilon(k)$ for $k = 0$ and $k = 1$ corresponds to the error of the first-order vegetation isoline and the asymmetric-order vegetation isoline without optimization, respectively. More than 9261 values of k were obtained using Equation (15), and each k was used to compute ϵ for 9261 patterns of the reflectance spectra. A two-dimensional array of ϵ values with a size of 9261 (spectral dimension) $\times$ 9261 (k-value dimension) was obtained. Figure 5 plots the values of ϵ averaged along the spectral dimensions as a function of the k-values. The error ϵ decreased until the k-value reached 1.25–1.30 and changed to an increasing function upon further increases in the k-value.
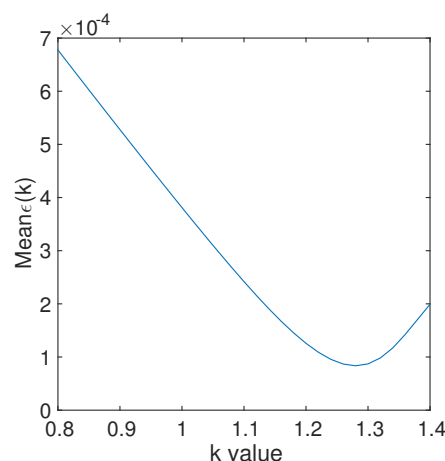
Figure 5. Plot of the mean value of ϵ versus the k-value.

The optimum values of k, k_{opt} were identified as follows: Six variations in the k-value were assumed: 1.25, 1.26, 1.27, 1.28, 1.29, and 1.30; the errors were approximated using the 9261 spectral patterns, that is, ϵ were computed for each k-value. The mean, standard deviation (STD), and maximum of ϵ for each k-value were computed and are summarized in Table 2. The minimum values of the mean

ϵ were 8.35×10^{-5} for $k = 1.28$. The values of the STD for $k = 1.29$ were, however, smaller than those obtained for $k = 1.28$. The same applied to the maximum. Accordingly, the optimum k-value, k_{opt}, was determined to be 1.29 for the Spherical LAD in this study.

Table 2. Statistics of $\epsilon(k)$ for k = 1.25, 1.26, 1.27, 1.28, 1.29, and 1.30. STD: standard deviation.

	LAD: Spherical					
	1.25	1.26	1.27	1.28	1.29	1.30
Mean	9.06×10^{-5}	8.68×10^{-5}	8.44×10^{-5}	8.35×10^{-5}	8.43×10^{-5}	8.71×10^{-5}
STD	1.08×10^{-4}	9.54×10^{-5}	8.44×10^{-5}	7.58×10^{-5}	7.05×10^{-5}	6.89×10^{-5}
MAX	7.05×10^{-4}	6.36×10^{-4}	5.66×10^{-4}	4.97×10^{-4}	4.31×10^{-4}	3.66×10^{-4}

4.5. Evaluation of $k_{opt} = 1.29$

The validity of using $k_{opt} = 1.29$ was then evaluated using contour plots of ϵ over LAI and R_{sR} space, holding FVC fixed at unity. Four variations of k (1.0, 1.25, 1.29, and 1.30) were considered. In Figure 6a, the minimum value of ϵ for $k = 1.0$ was 0.0002, and the errors were greater than those obtained under other conditions, as shown in Figure 6. Figure 6b presents results obtained for $k = 1.25$ and reveals that ϵ was less than 0.00015 for $R_{sR} < 0.26$. ϵ, however, it increased with increasing R_{sR}, especially for $R_{sR} > 0.26$ and for LAI approaching 1.0. Figure 6c shows that for $k = 1.29$, the maximum of ϵ was approximately 0.00025. Overall, ϵ was small across the entire parameter space. The results of ϵ obtained for $k = 1.30$ were slightly larger than the values obtained for $k = 1.29$ although ϵ was small for $R_{sR} > 0.26$.

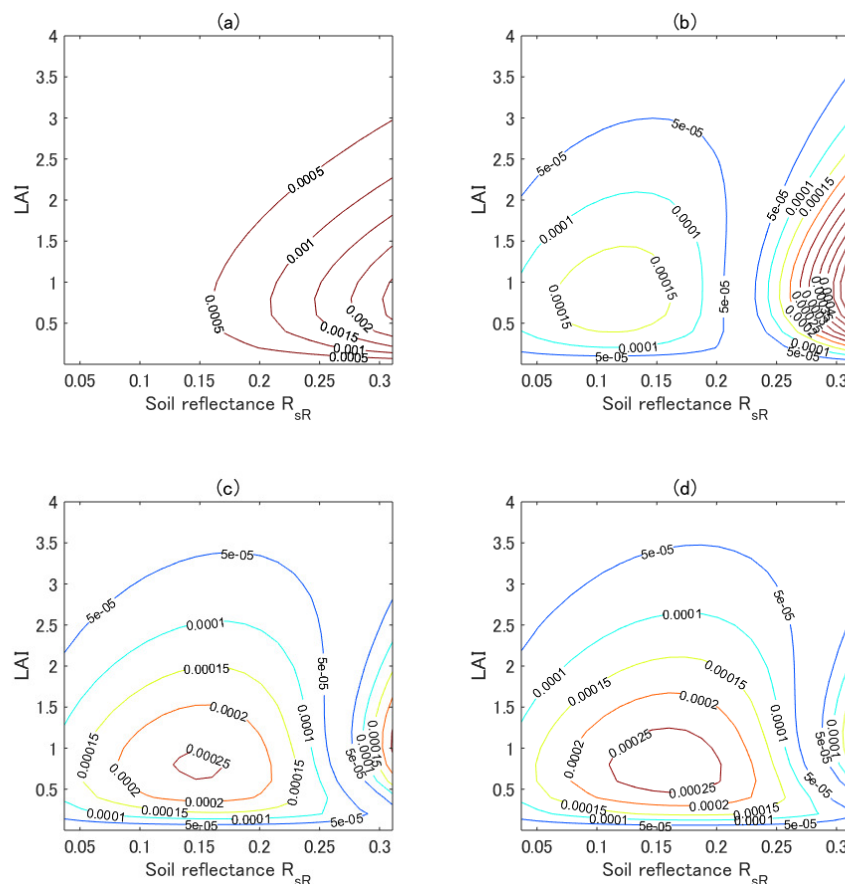**Figure 6.** (**a**) Contour plot of ϵ over LAI and R_{sR} space for $k = 1.00$; (**b**) Contour plot of ϵ for $k = 1.25$; (**c**) Contour plot of ϵ for $k = 1.29$; (**d**) Contour plot of ϵ for $k = 1.30$.

The error across the entire parameter space (e.g., the mean value of ϵ) was smallest for $k = 1.29$ (Figure 6c and Table 2), although ϵ for $k = 1.25$ was less than the value obtained for other k-values for $R_{sR} < 0.26$ (Figure 6b), and ϵ was smallest for $k = 1.30$ for $R_{sR} > 0.26$ (Figure 6d). This experiment, therefore, validated the use of the optimum k-value, k_{opt} (=1.29) for minimizing the overall error in the predicted NIR reflectances based on the adjusted asymmetric isoline equation. Furthermore, the value of ϵ for $k_{opt} = 1.29$, as shown in Figure 6c, was small relative to the noise equivalent error (0.0005).

We next computed the statistical profile of the errors in the first-order, the asymmetric-order, and the adjusted asymmetric-order ($k_{opt} = 1.29$) isoline equations. Table 3 lists the mean, STD, and maximum approximation error in the isoline equations. The mean values of the errors for the adjusted asymmetric-order isoline equations were reduced to 4% and 22% of the value obtained from the first-order and the asymmetric-order isoline equations. Likewise, the STD and maximum of the errors in the adjusted asymmetric-order isoline equations were much smaller than those obtained from other isoline equations. The statistical distribution of the errors in the adjusted asymmetric isoline equations did not exceed the noise equivalent errors (0.0005), even in the case of the maximum error.

Table 3. Statistics of the errors in first-order, asymmetric-order, and adjusted asymmetric-order ($k_{opt} = 1.29$) isoline equations.

	First-Order	Asymmetric	Adjusted Asymmetric	adj./first	adj./asym.
			LAD: Spherical		
Mean	2.10×10^{-3}	3.81×10^{-4}	8.43×10^{-5}	4.0%	22.1%
STD	2.43×10^{-3}	5.06×10^{-4}	7.05×10^{-5}	2.9%	13.9%
MAX	1.35×10^{-2}	2.67×10^{-3}	4.31×10^{-4}	3.2%	16.1%

4.6. Evaluation of $k_{opt} = 1.29$ for Various LADs and Variations in the Optimum k-Value

The performances of the derived isoline equations for $k_{opt} = 1.29$ were evaluated over various LADs in PROSAIL, including planophile, erectophile, plagiophile, extremophile, and uniform distributions, respectively. Table 4 lists the statistical analysis associated with approximating errors in the isoline equations (mean, STD, and maximum). The statistical distribution of the planophile was nearly identical to that of the Spherical model, as shown in Table 3. In other LADs, the statistical distributions of the derived equations were nearly equal to or more than half of the corresponding distributions of the other isoline equations. Also, although the maximum errors could exceed the noise equivalent error (0.0005), the mean values of the errors were less than 0.0004 for all LADs. This fact indicated that the adjusted asymmetric isoline equations with $k_{opt} = 1.29$ provided acceptable results, regardless of the choice of LAD.

The optimum values of k for the various LADs were explored using the algorithm presented in Section 4.4. The approximation errors ϵ with size of 9261 (spectral dimension) $\times$ 9261 (k-value dimension) were computed for each LAD, and the values of ϵ averaged along the spectral dimensions were computed and plotted as a function of the k-value for each LAD. Figure 7 plots the mean ϵ versus k-value for the various LADs. The k-values that provided the minimum value of the mean ϵ were approximately 1.2–1.3, except for the erectophile model, indicating that the minimum value of the mean ϵ occurred for $k > 1.5$.

Table 5 lists the optimum k-value and mean, STD, and maximum ϵ, where $\hat{\rho}_N$ was computed using the optimum k-value for each LAD obtained in our simulations. The mean values of the errors were approximately equal to or smaller than 0.0001. The magnitude of the STD of the errors was similar to that of mean. The maximum value of the errors was less than the noise equivalent error (0.0005), except for the erectophile model. The appropriate selection of the optimum k-value thus led to an accurate prediction of the NIR reflectances, but the use of $k_{opt} = 1.29$ provided an acceptable accuracy in terms of the SNR, even though this accuracy was not optimal for each LAD.

Table 4. Statistical distributions of the errors in the first-order, asymmetric-order, and adjusted aymmetric-order (k_{opt} = 1.29) isoline equations for the five LADs, including planophile, erectophile, plagiophile, extremophile, and uniform distributions.

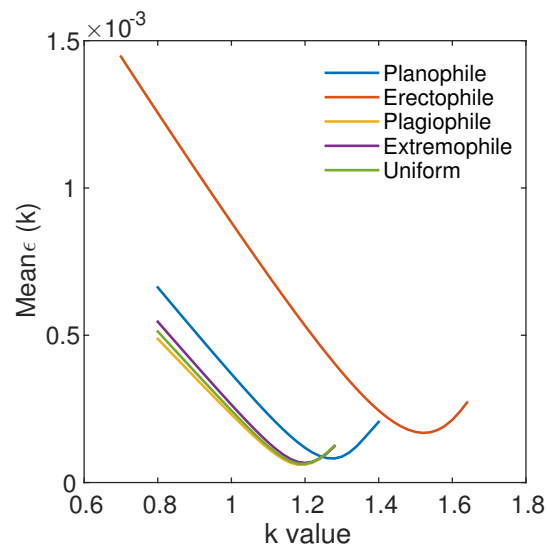|	LAD: Planophile				
	first-order isoline	asymmetric isoline	adjusted isoline	adj./1st	adj./asym.
Mean	2.07×10^{-3}	3.69×10^{-4}	8.39×10^{-5}	4.1%	22.7%
STD	2.40×10^{-3}	4.91×10^{-4}	6.76×10^{-5}	2.8%	13.8%
MAX	1.34×10^{-2}	2.59×10^{-3}	3.79×10^{-4}	2.8%	14.6%
	LAD: Erectophile				
	first-order isoline	asymmetric isoline	adjusted isoline	adj./1st	adj./asym.
Mean	3.08×10^{-3}	8.83×10^{-4}	3.89×10^{-4}	12.6%	44.1%
STD	3.54×10^{-3}	1.12×10^{-3}	5.53×10^{-4}	15.6%	49.4%
MAX	1.87×10^{-2}	5.79×10^{-3}	2.95×10^{-3}	15.8%	50.9%
	LAD: Plagiophile				
	first-order isoline	asymmetric isoline	adjusted isoline	adj./1st	adj./asym.
Mean	1.71×10^{-3}	2.31×10^{-4}	1.35×10^{-4}	7.9%	58.4%
STD	2.00×10^{-3}	3.15×10^{-4}	1.24×10^{-4}	6.2%	39.4%
MAX	1.13×10^{-2}	1.62×10^{-3}	7.78×10^{-4}	6.9%	48.0%
	LAD: Extremophile				
	first-order isoline	asymmetric isoline	adjusted isoline	adj./1st	adj./asym.
Mean	1.89×10^{-3}	2.64×10^{-4}	1.37×10^{-4}	7.2%	51.9%
STD	2.19×10^{-3}	3.57×10^{-4}	1.20×10^{-4}	5.5%	33.6%
MAX	1.23×10^{-2}	1.84×10^{-3}	7.04×10^{-4}	5.7%	38.3%
	LAD: Uniform				
	first-order isoline	asymmetric isoline	adjusted isoline	adj./1st	adj./asym.
Mean	1.79×10^{-3}	2.44×10^{-4}	1.38×10^{-4}	7.7%	56.6%
STD	2.09×10^{-3}	3.32×10^{-4}	1.24×10^{-4}	5.9%	37.3%
MAX	1.17×10^{-2}	1.71×10^{-3}	7.60×10^{-4}	6.5%	44.4%

Figure 7. Plot of the mean ϵ as a function of the *k*-value for the planophile, erectophile, plagiophile, extremophile, and uniform LADs, respectively.

Table 5. Optimum *k*-value and statistical distributions of the errors in the adjusted asymmetric isoline equations, with the optimal *k*-values for each of the five LADs, including the planophile, erectophile, plagiophile, extremophile, and uniform distributions.

LAD	Optimum *k*	Mean	STD	MAX
Planophile	1.28	8.17×10^{-5}	7.03×10^{-5}	4.44×10^{-4}
Erectophile	1.53	1.69×10^{-4}	1.39×10^{-4}	8.31×10^{-4}
Plagiophile	1.19	5.99×10^{-5}	6.23×10^{-5}	4.08×10^{-4}
Extremophile	1.2	6.65×10^{-5}	6.67×10^{-5}	4.40×10^{-4}
Uniform	1.20	6.31×10^{-5}	6.01×10^{-5}	3.81×10^{-4}

4.7. Comparison with the Noise-Equivalent Errors in Satellite Sensors

This study sought to decrease the errors associated with predicting the NIR reflectances by using red reflectances in the vegetation isoline equations. The goal was to decrease the errors to the level of the intrinsic errors of the sensor SNR values. Therefore, the errors in the first-order, the asymmetric-order, and the adjusted asymmetric isoline equations with $k_{opt} = 1.29$ were compared with the error arising from the SNR of the earth observation sensors currently in space orbit. We employed the SNRs of four sensors, including the Aqua-Moderate Resolution Imaging Spectroradiometer (MODIS) [34], the Landsat 8-Operational Land Imager (OLI) [35], the Greenhouse Gases Observing Satellite (GOSAT)-Cloud and Aerosol Imager (CAI) [36], and the Suomi National Polar-orbiting Partnership (SNPP)-Visible Infrared Imaging Radiometer Suite (VIIRS) [37], as summarized in Table 6.

Table 6. SNR in the red and NIR bands for the Aqua-Moderate Resolution Imaging Spectroradiometer (Aqua-MODIS) [38], Landsat 8-Operational Land Imager (Landsat 8 OLI) [39], Greenhouse Gases Observing Satellite (GOSAT)-Cloud and Aerosol Imager (CAI) [40], and Suomi National Polar-orbiting Partnership (NPP)-Visible Infrared Imaging Radiometer Suite (VIIRS) [41]. SNR for MODIS band1 (red) was derived by calculating 128 (sensor design requirement) × 1.57 (ratio of measured SNR in-orbit to sensor design requirement) and SNR for MODIS band 2 (NIR) was derived by 201 × 2.64 [38]. Similaly, SNR for VIIRS I1 and I2 bands (red and NIR) were derived by caluculating 119 × 1.76 and 150 × 1.5, respectively [41].

	MODIS	Landsat8 OLI	GOSAT-CAI	VIIRS
Red band	201	227	200	209
NIR band	530	201	200	225

The ratio of the relative errors in the isoline equations to the sensor SNR (*r*) was computed according to:

$$r = \frac{\epsilon(k)}{(\rho_N / SNR)} \tag{18}$$

The isoline equations were superior to the noise equivalent errors for values of less than unity, whereas the equations were inferior to the noise equivalent errors for values greater than unity. For comparison, the FVC and LAD were fixed, respectively, to unity and spherical.

Figure 8 plots *r* over the LAI-R_{sR} space. Thicker black lines correspond to *r* = 1.0. MODIS, OLI, CAI, and VIIRS correspond to the four rows of Figure 8 from the top to the bottom. From the left to the right column, the results of the first-order, asymmetric-order, and adjusted asymmetric-order isoline equations are plotted. The results of first-order isoline equations (Figure 8a,d,g,j) indicate that *r* exceeded unity over a large area of parameter space. The asymmetric-order isoline equations resulted in smaller values of *r* and exceeded unity for relatively large values of R_{sR}; however, the areas of these parts were significantly smaller than the area observed in the first-order isoline, as shown in Figure 8b,e,h,k. Finally, the results of *r* obtained from the adjusted asymmetric-order isoline equations

(Figure 8c,f,i,l) revealed that *r* never exceeded unity, and the maximum values of *r* were less than 0.5 for all sensors. In summary, the errors in the adjusted asymmetric isoline equations with $k_{opt} = 1.29$ were smaller than the error arising from the SNR of the four earth observation sensors.
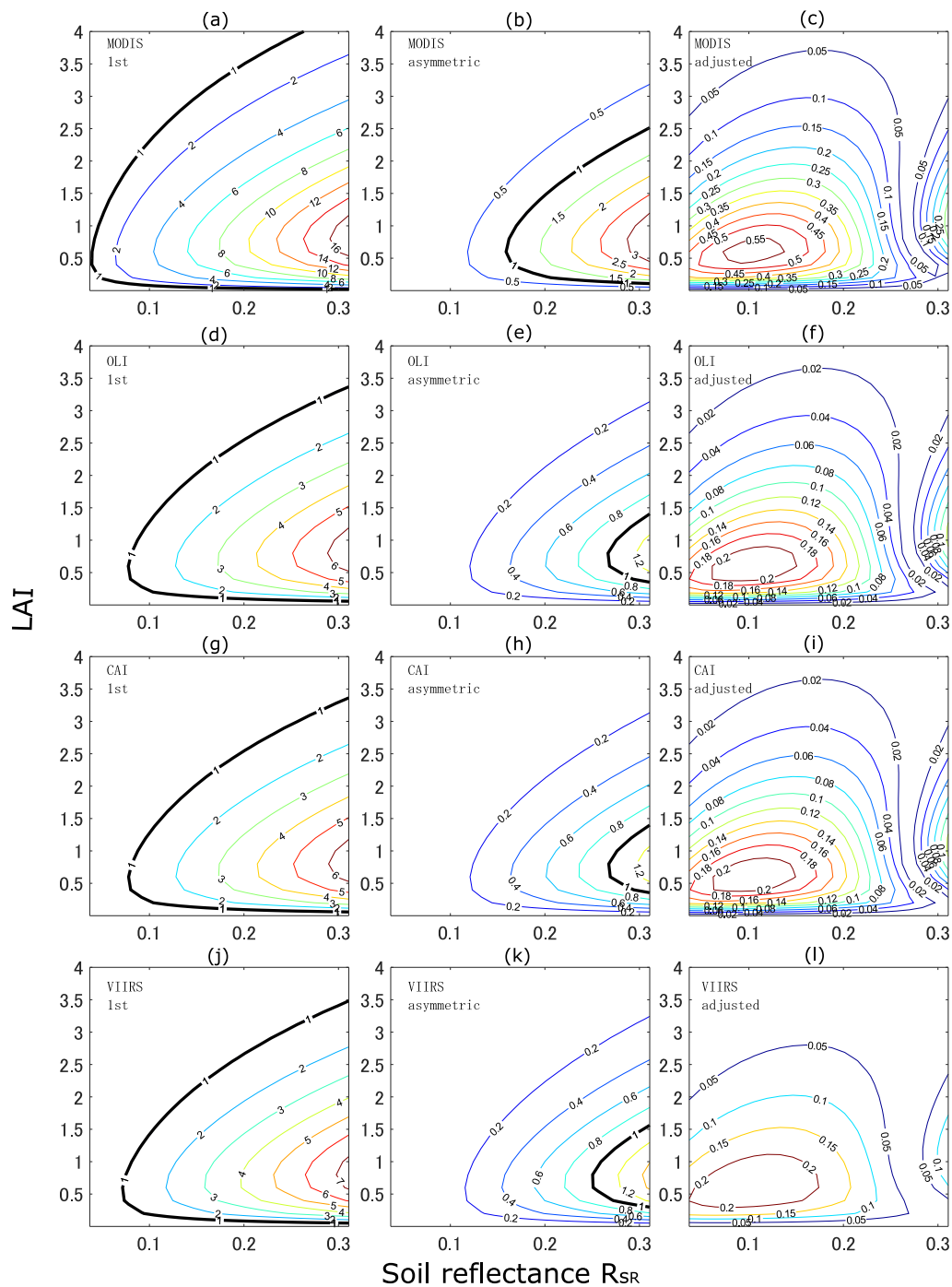

Figure 8. Contour plots of *r* over LAI-R_{sr} space. From the top to the bottom, each plot correspond to the MODIS (a, b, c), OLI (d, e, f), CAI (g, h, i), and VIIRS (j, k, l) sensors, respectively. From the left to right column, each plot corresponds to the first-order (a, d, g, j), asymmetric-order (b, e, h, k), and adjusted asymmetric-order (c, f, i, l) (with $k_{opt} = 1.29$) isoline equations, respectively. The bold line indicates *r* = 1.0. (**a**) MODIS-first; (**b**) MODIS-asymmetric; (**c**) MODIS-adjusted; (**d**) OLI-first; (**e**) OLI-asymmetric; (**f**) OLI-adjusted; (**g**) CAI-first; (**h**) CAI-asymmetric; (**i**) CAI-adjusted; (**j**) VIIRS-first; (**k**) VIIRS-asymmetric; (**l**) VIIRS-adjusted.

5. Discussion and Conclusions

The asymmetric-order isoline equations, derived from a previous study, were reformulated as first-order isoline equations plus a correction term multiplied by a parameter k. The derived equations with optimized k (as a constant) improved the accuracy of the asymmetric-order isoline equations while retaining the simplicity of the equations. The k-value was assumed to be a function of LAI, FVC, and R_{sR}, and the influences of R_{sR} on k were much greater than the influences of LAI and FVC such that k could be considered primarily to be a function of R_{sR}. One advantage of the isoline equations was that the parameters in the equations were independent of the soil brightness, i.e., R_{sR}; therefore, we fixed the k-value to an optimum instead of varying this parameter as a function of R_{sR}.

The errors in the adjusted asymmetric-order isoline equations were computed using k_{opt}. The errors in the reflectances predicted by the adjusted asymmetric-order isoline equations with k_{opt} were 4% and 22% of the errors predicted using the first-order and asymmetric-order isoline equations, respectively.

The value of k_{opt} was optimal for the Spherical LAD. The adjusted asymmetric-order isoline equations with k_{opt} reduced the errors significantly in the reflectances calculated using any of the six LADs defined in this study (less than half of the errors for the asymmetric-order isoline equations), although the use of the optimal k-value along with each LAD reduced the errors more significantly. In addition, the errors in the adjusted asymmetric-order isoline equations were small over the entire parameter space relative to the noise equivalent errors computed from the SNR of the satellite sensors currently in orbit (Aqua-MODIS, Landsat 8-OLI, SNPP-VIIRS, and GOSAT-CAI). The first-order and asymmetric-order isoline equations displayed both superiority and inferiority to the noise equivalent errors by relying on the canopy and soil conditions.

This study achieved its goal of reducing the error in the adjusted asymmetric-order isoline equations using a fixed k-value, yielding an error that was less than the noise equivalent errors based on the SNRs of some major satellite sensors, without complicating the isoline equations. Validation of the derived equations would require additional numerical experiments involving the application of other radiative transfer models of the vegetation canopy. Improved accuracy in the equations may be necessary if the sensor's SNR were to increase as a result of technological advancements in the sensor instrument design.

Author Contributions: Munenori Miura, Kenta Obata, and Hiroki Yoshioka designed the concept of this study, developed the improvement technique, and conducted the numerical experiments. Kenta Taniguchi validated the Matlab scripts used in this study. Kenta Taniguchi contributed also to the interpretation of results and editing the manuscripts.

Conflicts of Interest: The authors declare no conflict of interest.

References

1.	Miura, T.; Huete, A.R. Performance of three reflectance calibration methods for airborne hyperspectral spectrometer data. *Sensors* **2009**, *9*, 794–813.
2.	Miura, T.; Yoshioka, H.; Fujiwara, K.; Yamamoto, H. Inter-comparison of ASTER and MODIS surface reflectance and vegetation index products for synergistic applications to natural resource monitoring. *Sensors* **2008**, *8*, 2480–2499.
3.	Fan, X.; Liu, Y. A Generalized Model for Intersensor NDVI Calibration and Its Comparison With Regression Approaches. *IEEE Trans. Geosci. Remote Sens.* **2016**, *PP*, 1–11.
4.	Zhu, Z.; Bi, J.; Pan, Y.; Ganguly, S.; Anav, A.; Xu, L.; Samanta, A.; Piao, S.; Nemani, R.R.; Myneni, R.B. Global Data Sets of Vegetation Leaf Area Index (LAI)3g and Fraction of Photosynthetically Active Radiation (FPAR)3g Derived from Global Inventory Modeling and Mapping Studies (GIMMS) Normalized Difference Vegetation Index (NDVI3g) for the Period 1981 to 2011. *Remote Sens.* **2013**, *5*, 927.

5. Hansen, M.C.; Potapov, P.V.; Moore, R.; Hancher, M.; Turubanova, S.A.; Tyukavina, A.; Thau, D.; Stehman, S.V.; Goetz, S.J.; Loveland, T.R.; et al. High-Resolution Global Maps of 21st-Century Forest Cover Change. *Science* **2013**, *342*, 850–853.

6. Qin, J.; Liang, S.; Li, X.; Wang, J. Development of the adjoint model of a canopy radiative transfer model for sensitivity study and inversion of leaf area index. *IEEE Trans. Geosci. Remote Sens.* **2008**, *46*, 2028–2037.

7. Vina, A.; Gitelson, A.A.; Nguy-Robertson, A.L.; Peng, Y. Comparison of different vegetation indices for the remote assessment of green leaf area index of crops. *Remote Sens. Environ.* **2011**, *115*, 3468–3478.

8. Huete, A.R. A soil-adjusted vegetation index (SAVI). *Remote Sens. Environ.* **1988**, *25*, 295–309.

9. Baret, F.; Guyot, G.; Major, D. TSAVI: A vegetation index which minimizes soil brightness effects on LAI and APAR estimation. In Proceedings of the 1989 International 12th Canadian Symposium on Remote Sensing Geoscience and Remote Sensing Symposium, Vancouver, BC, Canada, 10–14 July 1989; Volume 3, pp. 1355–1358.

10. Kaufman, Y.J.; Tanre, D. Atmospherically resistant vegetation index (ARVI) for EOS-MODIS. *IEEE Trans. Geosci. Remote Sens.* **1992**, *30*, 261–270.

11. Huete, A.; Justice, C.; Liu, H. Development of vegetation and soil indices for MODIS-EOS. *Remote Sens. Environ.* **1994**, *49*, 224–234.

12. Gilabert, M.; González-Piqueras, J.; García-Haro, F.; Meliá, J. A generalized soil-adjusted vegetation index. *Remote Sens. Environ.* **2002**, *82*, 303–310.

13. Chen, D.; Huang, J.; Jackson, T.J. Vegetation water content estimation for corn and soybeans using spectral indices derived from MODIS near- and short-wave infrared bands. *Remote Sens. Environ.* **2005**, *98*, 225–236.

14. Matsushita, B.; Yang, W.; Chen, J.; Onda, Y.; Qiu, G. Sensitivity of the Enhanced Vegetation Index (EVI) and Normalized Difference Vegetation Index (NDVI) to Topographic Effects: A Case Study in High-density Cypress Forest. *Sensors* **2007**, *7*, 2636–2651.

15. Jiang, Z.; Huete, A.R.; Didan, K.; Miura, T. Development of a two-band enhanced vegetation index without a blue band. *Remote Sens. Environ.* **2008**, *112*, 3833–3845.

16. Verstraete, M.M.; Pinty, B. Designing optimal spectral indexes for remote sensing applications. *IEEE Trans. Geosci. Remote Sens.* **1996**, *34*, 1254–1265.

17. Yoshioka, H.; Miura, T.; Huete, A.; Ganapol, B. Analysis of vegetation isolines in red-NIR reflectance space. *Remote Sens. Environ.* **2000**, *74*, 313–326.

18. Yoshioka, H.; Miura, T.; Demattê, J.A.; Batchily, K.; Huete, A.R. Derivation of soil line influence on two-band vegetation indices and vegetation isolines. *Remote Sens.* **2009**, *1*, 842–857.

19. Yoshioka, H.; Yamamoto, H.; Miura, T. Use of an isoline-based inversion technique to retrieve a leaf area index for inter-sensor calibration of spectral vegetation index. In Proceedings of the International Geoscience and Remote Sensing Symposium, Toronto, ON, Canada, 24–28 June 2002; Volume 3, pp. 1639–1641.

20. Kallel, A.; Le Hégarat-Mascle, S.; Ottlé, C.; Hubert-Moy, L. Determination of vegetation cover fraction by inversion of a four-parameter model based on isoline parametrization. *Remote Sens. Environ.* **2007**, *111*, 553–566.

21. Yoshioka, H.; Miura, T.; Obata, K. Derivation of relationships between spectral vegetation indices from multiple sensors based on vegetation isolines. *Remote Sens.* **2012**, *4*, 583–597.

22. Obata, K.; Miura, T.; Yoshioka, H.; Huete, A.R. Derivation of a MODIS-compatible enhanced vegetation index from visible infrared imaging radiometer suite spectral reflectances using vegetation isoline equations. *J. Appl. Remote Sens.* **2013**, *7*, 073467.

23. Miura, M.; Obata, K.; Yoshioka, H. Vegetation isoline equations with first-and second-order interaction terms for modeling a canopy-soil system of layers in the red and near-infrared reflectance space. *J. Appl. Remote Sens.* **2015**, *9*, 095987.

24. Jacquemoud, S.; Baret, F.; Andrieu, B.; Danson, F.; Jaggard, K. Extraction of vegetation biophysical parameters by inversion of the PROSPECT+ SAIL models on sugar beet canopy reflectance data. Application to TM and AVIRIS sensors. *Remote Sens. Environ.* **1995**, *52*, 163–172.

25. Jacquemoud, S.; Verhoef, W.; Baret, F.; Bacour, C.; Zarco-Tejada, P.J.; Asner, G.P.; François, C.; Ustin, S.L. PROSPECT+ SAIL models: A review of use for vegetation characterization. *Remote Sens. Environ.* **2009**, *113*, S56–S66.

26. Yoshioka, H.; Huete, A.R.; Miura, T. Derivation of vegetation isoline equations in red-NIR reflectance space. *IEEE Trans. Geosci. Remote Sens.* **2000**, *38*, 838–848.

27. Yoshioka, H.; Miura, T.; Huete, A.R. An isoline-based translation technique of spectral vegetation index using EO-1 Hyperion data. *IEEE Trans. Geosci. Remote Sens.* **2003**, *41*, 1363–1372.

28. Yoshioka, H. Vegetation isoline equations for an atmosphere-canopy-soil system. *IEEE Trans. Geosci. Remote Sens.* **2004**, *42*, 166–175.

29. Miura, M.; Obata, K.; Yoshioka, H. Vegetation isoline equations for analysis of hyper-spectral data with higher order interaction terms. In Proceedings of the International Geoscience and Remote Sensing Symposium (IGARSS), Honolulu, HI, USA, 25–30 July 2010; pp. 1031–1034.

30. Miura, M.; Obata, K.; Yoshioka, H. Vegetation isoline equations for atmosphere-canopy-soil system of layer with second order interaction term. In Proceedings of the SPIE Optical Engineering+ Applications. International Society for Optics and Photonics, San Diego, CA, USA, 1–5 August 2010; p. 780906.

31. Obata, K.; Miura, T.; Yoshioka, H.; Huete, A.R.; Vargas, M. Spectral Cross-Calibration of VIIRS Enhanced Vegetation Index with MODIS: A Case Study Using Year-Long Global Data. *Remote Sens.* **2016**, *8*, 34.

32. Jacquemoud, S.; Baret, F. PROSPECT: A model of leaf optical properties spectra. *Remote Sens. Environ.* **1990**, *34*, 75–91.

33. Verhoef, W. Light scattering by leaf layers with application to canopy reflectance modeling: The SAIL model. *Remote Sens. Environ.* **1984**, *16*, 125–141.

34. Justice, C.O.; Vermote, E.; Townshend, J.R.; Defries, R.; Roy, D.P.; Hall, D.K.; Salomonson, V.V.; Privette, J.L.; Riggs, G.; Strahler, A.; et al. The Moderate Resolution Imaging Spectroradiometer (MODIS): Land remote sensing for global change research. *IEEE Trans. Geosci. Remote Sens.* **1998**, *36*, 1228–1249.

35. Roy, D.P.; Wulder, M.; Loveland, T.; Woodcock, C.; Allen, R.; Anderson, M.; Helder, D.; Irons, J.; Johnson, D.; Kennedy, R.; et al. Landsat-8: Science and product vision for terrestrial global change research. *Remote Sens. Environ.* **2014**, *145*, 154–172.

36. Yokota, T.; Yoshida, Y.; Eguchi, N.; Ota, Y.; Tanaka, T.; Watanabe, H.; Maksyutov, S. Global concentrations of $CO2$ and $CH4$ retrieved from GOSAT: First preliminary results. *Sola* **2009**, *5*, 160–163.

37. Cao, C.; Xiong, J.; Blonski, S.; Liu, Q.; Uprety, S.; Shao, X.; Bai, Y.; Weng, F. Suomi NPP VIIRS sensor data record verification, validation, and long-term performance monitoring. *J. Geophys. Res.* **2013**, *118*, 11664–11678.

38. Xiong, X.; Sun, J.; Xie, X.; Barnes, W.L.; Salomonson, V.V. On-Orbit Calibration and Performance of Aqua MODIS Reflective Solar Bands. *IEEE Trans. Geosci. Remote Sens.* **2010**, *48*, 535–546.

39. Morfitt, R.; Barsi, J.; Levy, R.; Markham, B.; Micijevic, E.; Ong, L.; Scaramuzza, P.; Vanderwerff, K. Landsat-8 Operational Land Imager (OLI) Radiometric Performance On-Orbit. *Remote Sens.* **2015**, *7*, 2208.

40. Fukuda, S.; Nakajima, T.; Takenaka, H.; Higurashi, A.; Kikuchi, N.; Nakajima, T.Y.; Ishida, H. New approaches to removing cloud shadows and evaluating the 380 nm surface reflectance for improved aerosol optical thickness retrievals from the GOSAT/TANSO-Cloud and Aerosol Imager. *J. Geophys. Res.* **2013**, *118*, 13,520–13,531.

41. Xiong, X.; Butler, J.; Chiang, K.; Efremova, B.; Fulbright, J.; Lei, N.; McIntire, J.; Oudrari, H.; Sun, J.; Wang, Z.; Wu, A. VIIRS on-orbit calibration methodology and performance. *J. Geophys. Res.* **2014**, *119*, 5065–5078.